



HAL
open science

In silico assessment of the effects of various compounds in MEA/hiPSC-CM assays: Modelling and numerical simulations

Emanuela Abbate, Muriel Boulakia, Yves Coudière, Jean-Frédéric Gerbeau, Philippe Zitoun, Nejib Zemzemi

► To cite this version:

Emanuela Abbate, Muriel Boulakia, Yves Coudière, Jean-Frédéric Gerbeau, Philippe Zitoun, et al.. In silico assessment of the effects of various compounds in MEA/hiPSC-CM assays: Modelling and numerical simulations. *Journal of Pharmacological and Toxicological Methods*, 2018, 89, pp.59-72. hal-01562673

HAL Id: hal-01562673

<https://inria.hal.science/hal-01562673>

Submitted on 16 Jul 2017

HAL is a multi-disciplinary open access archive for the deposit and dissemination of scientific research documents, whether they are published or not. The documents may come from teaching and research institutions in France or abroad, or from public or private research centers.

L'archive ouverte pluridisciplinaire **HAL**, est destinée au dépôt et à la diffusion de documents scientifiques de niveau recherche, publiés ou non, émanant des établissements d'enseignement et de recherche français ou étrangers, des laboratoires publics ou privés.

In silico assessment of the effects of various compounds in MEA/hiPSC-CM assays: Modelling and numerical simulations

E. Abbate, M. Boulakia, Y. Coudière, J-F. Gerbeau, P. Zitoun and N. Zenzemi

Abstract

We propose a mathematical approach for the analysis of drugs effects on the electrical activity of human induced pluripotent stem cell-derived cardiomyocytes (hiPSC-CMs) based on multi-electrode array (MEA) experiments. Our goal is to produce an *in silico* tool able to simulate drugs action in MEA/hiPSC-CM assays. The mathematical model takes into account the geometry of the MEA and the electrodes' properties. The electrical activity of the stem cells at the ion-channel level is governed by a system of ordinary differential equations (ODEs). The ODEs are coupled to the bidomain equations, describing the propagation of the electrical wave in the stem cells preparation. The field potential (FP) measured by the MEA is modeled by the extra-cellular potential of the bidomain equations. First, we propose a strategy allowing us to generate a field potential in good agreement with the experimental data. We show that we are able to reproduce realistic field potentials by introducing different scenarios of heterogeneity in the action potential. This heterogeneity reflects the differentiation atria/ventricles and the age of the cells. Second, we introduce a drug/ion channels interaction based on a pore block model. We conduct different simulations for five drugs (mexiletine, dofetilide, bepridil, ivabradine and BayK). We compare the simulation results with the field potential collected from experimental measurements. Different biomarkers computed on the FP are considered, including depolarization amplitude, repolarization delay, repolarization amplitude and depolarization-repolarization segment. The simulation results show that the model reflect properly the main effects of these drugs on the FP.

Keywords: Cardiac electrophysiology, MEA, field potential, drug modelling, hiPSC-CMs.

1. Introduction

Recent studies on stem cells showed that it is possible to induce pluripotency, i.e. the capability of differentiating into all tissues of an organism [1]. Stem cell-derived cardiomyocytes (CMs) appear as a promising tool in regenerative medicine, for example to restore the cardiac function after an infarct [2, 3].

Human induced pluripotent stem cells (hiPSCs) are considered in this work. These cells are derived by reprogramming somatic cells and can be cultivated in the pluripotency state or differentiated into somatic cell types, including CMs [4]. Until now, the knowledge regarding the cardiac tissue mainly relied on animal models, like dog, rabbit or guinea pig. Today, many types of human pluripotent stem cells are investigated for their potential to produce functional CMs [5, 6]. hiPSC-CMs are valuable models because of their resemblance to adult myocytes, especially in the electrophysiological behavior [7]. Therefore, the role of hiPSC-CMs as *in vitro* models is becoming more and more important. In hiPSC-CMs preparations, a strong heterogeneity in the morphology of the action potentials is usually observed. However, the signals can be classified into three major types: nodal-like, embryonic atrial-like, and embryonic ventricular-like [5, 4].

The hiPSC-CMs have been used in different fields: toxicity testing, study of certain diseases, pharmacological response, drug design *etc.* [6, 4, 8, 9, 10, 11]. The present study is related to the problem of drug screening in safety pharmacology. Our goal is to model and simulate MEA measurements that are performed by pharmaceutical companies on hiPSC-CMs preparations. The aim of these experiments is to predict and test the main effects of a drug on the electrophysiology of cardiomyocytes. But the electrical signal collected by an MEA device, called the Field Potential (FP), is difficult to analyze, because of its variability, and because it has been much less studied than the Action Potential (AP). With this study, we want to show that mathematical modeling and numerical simulation can contribute to a better understanding of the MEA measurements. Some preliminary simulations of the FP were recently presented [12, 13, 14] and the modeling of drug effects, side effects and interactions was addressed in several works [15, 16, 17]. But to the best of our knowledge, the present article is the first *in silico* study of drug effects on the FP.

Here is a brief description of the methods adopted in this work. Our mathematical model is based on the bidomain equations, used in many works for the description of the electrical activity of the heart. In order to reproduce the electrical activity of hiPSC-CMs, a state-of-the-art ionic model describing the membrane activity of stem cells is used in Paci et al [18]. Since the experimental measurements are registered by MEA devices, a model of electrodes is introduced and coupled to the bidomain equations. The resulting equations allow us to model the field potential recorded by the MEA device. A specific device is considered (the 60-6 well MEA produced by the company Multi Channel Systems) but the methodology can be applied to other kinds of MEAs. This device is made of six independent wells. Each well contains nine electrodes (Fig. 1(a)). Six independent experiments can thus be done with identical surrounding conditions at once [19].

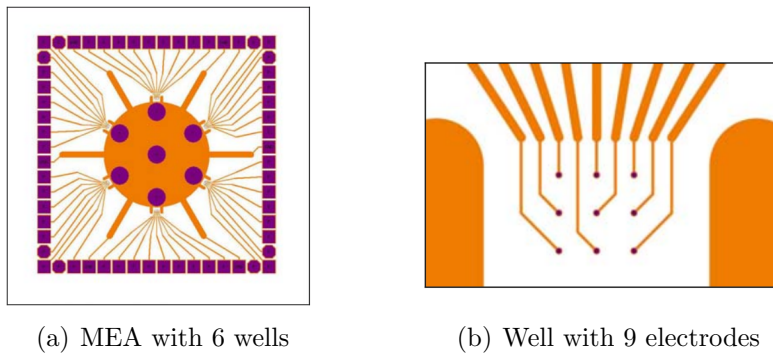


Figure 1: Multichannel Systems device [19]. Panel (a): 60-6well MEA device. Panel (b): zoom on one well with the 9 electrodes (reproduced with permission).

The geometry used for the computation is two-dimensional. It models one layer of cells in a well, as represented in Fig. 1(b). A special effort is dedicated to the modeling of the electrophysiological heterogeneity, which is a prominent characteristic of hiPSC-CMs preparations. This is done by introducing different phenotypes, atrial- and ventricular-like, and by varying the action potential amplitudes. Various configurations are generated following this approach. The *in silico* results corresponding to the different configurations are averaged and compared to *in vitro* experiments for five different drugs (mexiletine, dofetilide, bepridil, ivabradine and BayK).

The paper is organized as follows. In Section 2, the mathematical models of the field potential and the drug-channel interactions are presented. In Sec-

tion 3, the simulation results are presented and compared with experimental measurements. Section 4 is dedicated to a discussion and some concluding remarks.

2. Materials and Methods

In this section, the methodology of the study is detailed. First, a mathematical model is presented to reproduce the experimental field potential *in silico*. Then a strategy is proposed to reflect the strong variability observed in the experiments. The section ends with the approach used to model the action of compounds on the ion channels.

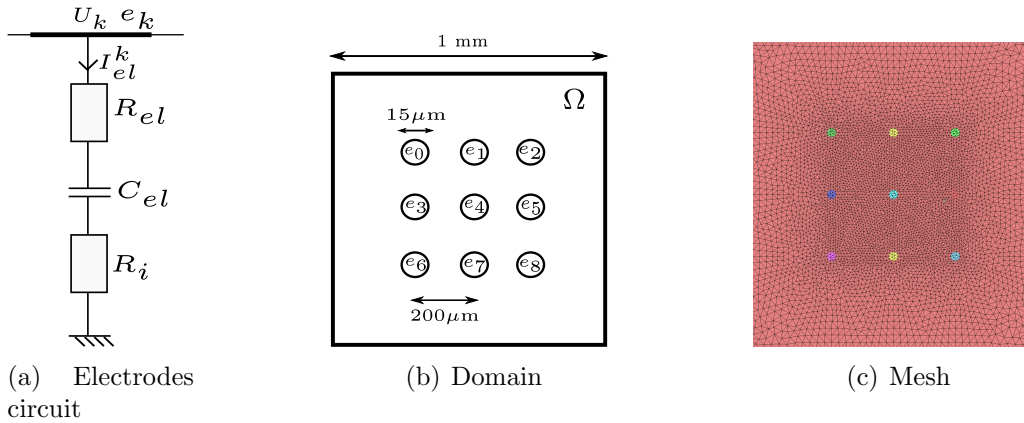


Figure 2: Schematic representation of the electrodes electrical circuit (a). 2D domain Ω with dimensions and positions of the 9 electrodes (b). Computational mesh representing a triangular discretization of the domain Ω with $h \approx 25 \mu\text{m}$ (c).

2.1. Electrophysiology of a monolayer of cells in a MEA

Since the culture of hiPSC-CMs is made of a monocellular layer, with a thickness z_{thick} much smaller than the other dimensions, the domain occupied by the cells in a well is assumed to be two-dimensional (Fig. 1(b)). It is denoted by Ω and is schematically represented in Fig. 2(b).

The electrical activity of the tissue is described using the bidomain equations, which result from the homogenization of a microscopic model that takes into account both the intracellular and the extracellular media. For a

detailed derivation of the bidomain model see for example [20, 21]. In the two-dimensional configuration of the MEA, these equations read:

$$\begin{cases} A_M \left(C_M \frac{\partial V_M}{\partial t} + I_{ion} \right) - \operatorname{div}(\sigma_I \nabla V_M) - \operatorname{div}(\sigma_I \nabla u_e) = A_M I_{stim} & \text{in } \Omega \text{a} \\ -\operatorname{div}((\sigma_I + \sigma_E) \nabla u_e) - \operatorname{div}(\sigma_I \nabla V_M) = \frac{1}{z_{thick}} \sum_{e_k} \frac{I_{el}^k}{|e_k|} \chi_{e_k} & \text{in } \Omega. \quad (1b) \\ \frac{d\mathbf{w}}{dt} - \mathbf{g}(V_M, \mathbf{w}) = 0 & \text{in } \Omega. \quad (1c) \end{cases}$$

where $|e_k|$ denotes the surface of the electrode k , and χ_{e_k} denotes its characteristic function, i.e. the function equal to one inside the electrode and zero outside. Functions V_M and u_e are respectively the transmembrane and extracellular potentials. The constant C_M is the transmembrane specific capacitance, A_M is the surface area of membrane per unit volume of tissue, σ_I and σ_E are respectively the intracellular and extracellular conductivities. The transmembrane ionic current I_{ion} is provided by the model proposed in Paci et al [18]. This ionic model, based on the Hodgkin-Huxley theory [22] and represented by Equation (1c), reproduces the activity of auto-excitable hiPSC-CMs. It includes the activity of several transmembrane channels and the intracellular calcium exchanges. The state variables vector \mathbf{w} consists of the concentrations of ions and the gate variables. The precise definition of function $\mathbf{g}(V_M, \mathbf{w})$ can be found in the appendix of [18]. In Equation (1a), the current I_{stim} is an external stimulation, which can be applied at a certain location of the domain for a certain duration. For the boundary conditions of the coupled problem, we impose that the flux of the intracellular potential ($V_M + u_e$) over the boundary is equal to zero

$$\sigma_I \nabla(V_M + u_e) \cdot \mathbf{n} = 0.$$

For the extracellular potential, we use homogeneous Dirichlet boundary conditions ($u_e = 0$) on three edges connected to the ground, which has a "U" shape as shown in Fig1(b). For the remaining edge, we use a non flux boundary condition $\sigma_E \nabla u_e \cdot \mathbf{n} = 0$.

Let us now explain the source term added in Equation (1b) to model the presence of the electrodes. In a three-dimensional description, the following boundary condition should be introduced in the regions where the electrodes

are located [23]:

$$\sigma_E \nabla u_e \cdot \mathbf{n} = \frac{I_{el}^k}{|e_k|} \quad \text{on } e_k, \quad (2)$$

where I_{el}^k is the electric current measured by the k^{th} electrode and computed using the electric model of Fig. 2(a), by solving the following ODE:

$$\frac{dI_{el}^k}{dt} + \frac{I_{el}^k}{\tau} = \frac{C_{el}}{\tau} \frac{dU^k}{dt} \quad \text{with } U^k = \frac{1}{|e_k|} \int_{e_k} u_e \, de_k, \quad (3)$$

where $\tau = (R_i + R_{el})C_{el}$, R_i standing for the ground resistance, R_{el} and C_{el} for the resistance and the capacitance of the electrode. In Eq. (3) we have introduced U^k as the mean value of the extracellular potential u_e over the electrode k .

Since the thickness of the monolayer of cells z_{thick} is supposed to be very small compared to the other dimensions of the problem, we assume that all the variations along the z -direction are negligible compared to the variations along the directions x and y . After some manipulations, condition (2) of the three-dimensional problem is transformed into the source term in the two-dimensional equation (1b). The field potential measured by electrode k is then computed as

$$U_{fp}^k = R_i I_{el}^k.$$

In Table 1, we provide the values of the macroscopic model parameters used in the simulations. For the tissue conductivity, we choose the values $\sigma_i = 10 \mu\text{S cm}^{-1}$ and $\sigma_e = 30 \mu\text{S cm}^{-1}$, in order to fit with the conduction velocity in the experimental data. These values are lower than conductivities in human cardiac tissue, due to the fact that in hiPSC-CMs the conduction velocity (CV) is much slower than in the human heart [6]. The CV obtained with the chosen conductivities is around 4cm/s. For the electrode model, we take a ground resistance $R_i = 10^9 \Omega$ and an electrode resistance of $R_{el} = 10^6 \Omega$. R_{el} was not introduced in the model provided in [23]. We introduce it in order to model as close to reality as possible the physical phenomena. Nevertheless, according to equation (3), the resistance R_{el} does not have any effect on the field potential since $R_i = 10^9 \Omega \gg R_{el}$. In [23], the authors prove that taking ground resistance values of $10^{12} \Omega$ and of $10^9 \Omega$ gives the same accuracy as a perfect electrode with infinite resistance. The value of C_{el} is in the range of manufacturer values provided in [23].

The system of partial differential equations is discretized in space with piecewise linear finite elements, and in time with a time stepping scheme [24].

We use a triangular mesh as shown in Figure 2(c). The full time and space numerical discretizations are given in the supplementary material, where we also provide a time convergence analysis. We have chosen the value of $\Delta t = 0.2\text{ms}$ in order to ensure a relative error lower than 1% on the action potential. The reference solution in this convergence analysis is obtained using a time step $\Delta t = 1\mu\text{s}$.

Parameter	Symbol	Value
Rate of membrane surface per volume [25]	A_M	1200 cm^{-1}
Membrane specific capacitance [25]	C_M	$1\text{ }\mu\text{F cm}^{-2}$
Intracellular conductivity	σ_I	$10\text{ }\mu\text{S cm}^{-1}$
Extracellular conductivity	σ_E	$30\text{ }\mu\text{S cm}^{-1}$
Electrodes capacitance [23]	C_{el}	10^{-10} F
Electrodes ground resistance [23]	R_i	$10^9\text{ }\Omega$
Electrodes internal resistance	R_{el}	$10^6\text{ }\Omega$
z thickness	z_{thick}	10^{-4} cm

Table 1: Values of the parameters used in the simulations.

In Figure 3, we plot the time course of the simulated field potential for the 9 electrodes. The tissue was stimulated at the bottom-left corner with $I_{stim} = 150\text{A/cm}^{-2}$. In this case, if we do not stimulate the tissue, all cells depolarize at the same time. The extra-cellular potential solution would then be equal to zero in the whole domain and the computed FP would also be equal to zero.

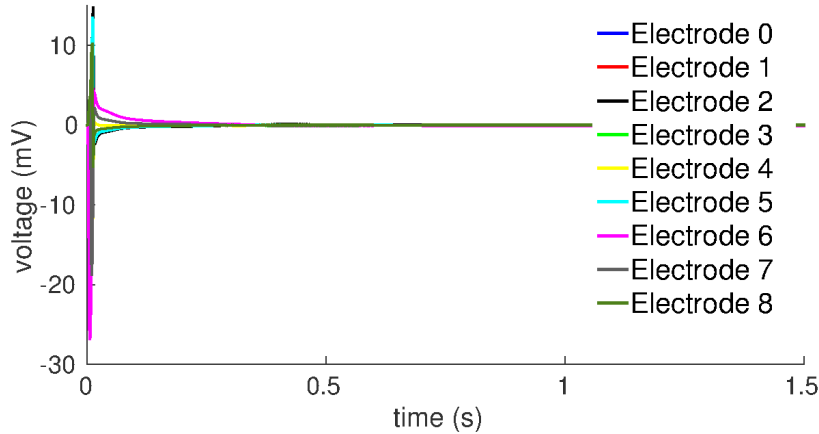


Figure 3: Simulated field potentials over the 9 electrodes for ventricular-like hiPSC-CM without introducing any heterogeneity in the model.

2.2. Handling the heterogeneity and the variability

2.2.1. Experimental observations and main hypotheses

The electrophysiological heterogeneity and variability are a prominent characteristic of stem cell preparations, as pointed out in different works [4, 6, 8, 26]. The heterogeneous behavior mainly comes from the intrinsic differences in the cell lines used in experiments and from the conditions under which the cells are differentiated. Patch-clamp measurements suggest a clas-

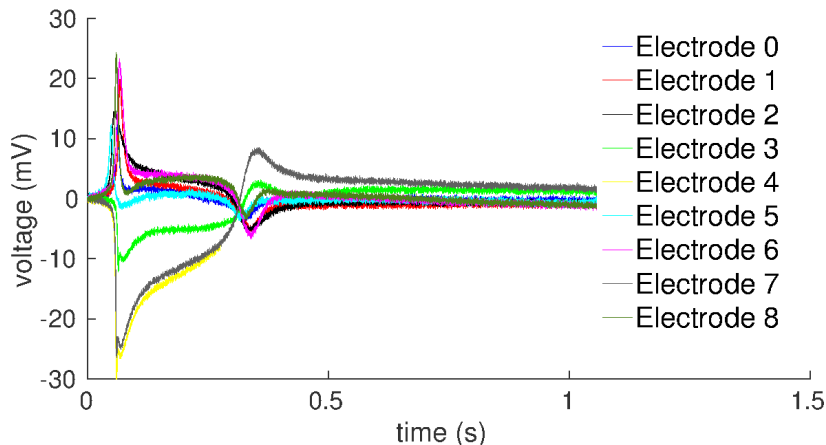
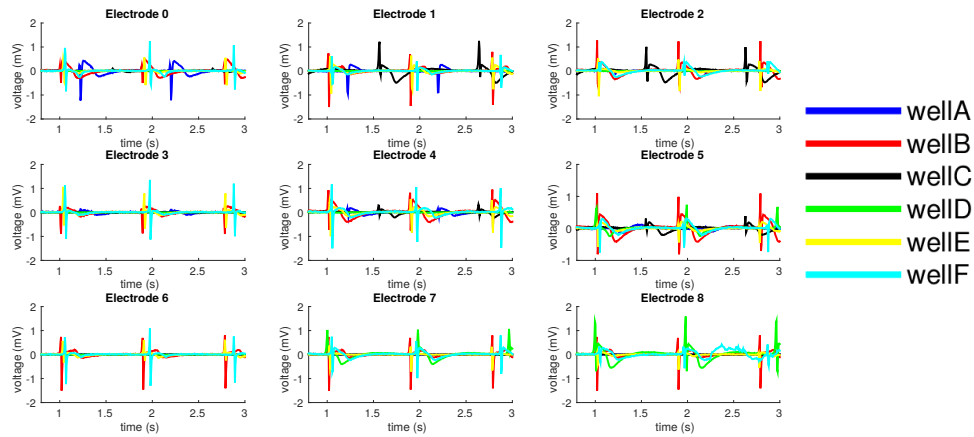


Figure 4: Field potential signals of the 9 electrodes recorded from one MEA well. The experimental measurements were produced by *Janssen / NMI* and provided by *Notocord*.

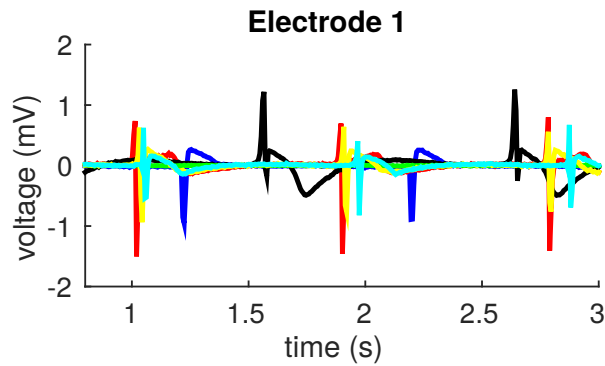
sification of the cells among three main phenotypes; atrial-, ventricular- and nodal-like. This classification is based on the comparison of their AP with adult cardiomyocytes' AP. Distinction between atrial and ventricular-like is usually based on the following biomarker [4, 6]:

$$RO = \frac{APD_{30-40}}{APD_{70-90}} \begin{cases} \leq 1.5 & \text{atrial-like} \\ > 1.5 & \text{ventricular-like,} \end{cases}$$

where APD stands for action potential duration. This ratio measures the slope at the beginning of repolarization. A triangular shaped AP is classified as atrial-like. But still inside a phenotype, we observe large variations in the AP morphologies. For instance in [4], the variations of biomarkers such as AP amplitude, firing velocity and APD_{90} inside each phenotype are studied and quantified. In a MEA well, the field potential signals collected by the electrodes at different locations are different in shape and behavior.



(a) 6 wells



(b) Zoom on electrode 1

Figure 5: *In vitro* data: Panel (a): field potential signals of 6 MEA wells (each one with 9 electrodes). Zoom on electrode number one (c)

For instance, Fig. 4 shows the 9 experimental FPs in a MEA well: shape differences are striking. In Fig. 5(a), the results of a MEA experiment are presented: in the same environment conditions, the signals collected in the six wells exhibit great differences in amplitude, shape and frequency.

The *in silico* signals given by the model (1a)-(3) are reported in Figure 3 are not in a good agreement with the experimental signals. Conjecturing that the discrepancy is due to the absence of heterogeneity in the *in silico* model, we will enrich our model with some new features detailed in the next subsections.

2.2.2. Modeling different phenotypes

In [18], the authors propose atrial- and ventricular-like ionic models: the main differences concern some channels conductances and the I_{CaL} dynamics, which is the main responsible for the plateau phase. As a first attempt at modeling the electrophysiological heterogeneity, we introduce the two phenotypes in the same hiPSC-CMs preparation. The original domain is split into two different parts, as in the simple configuration of Fig. 6: $\Omega = \Omega_1 \cup \Omega_2$. Ventricular-like cells being the predominant phenotype [4], the ventricular model is solved in Ω_1 and the atrial model in Ω_2 . As will be shown in Sec-

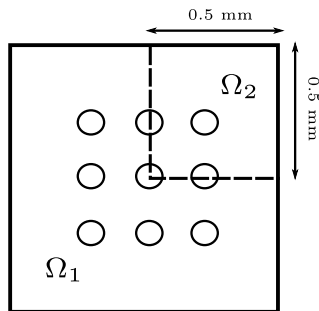


Figure 6: Splitting of the domain Ω into two different regions Ω_1 and Ω_2 .

tion 3, this strategy is not sufficient to qualitatively match the experimental signals, especially during the plateau phase. Recalling that the presence of two phenotypes mainly affect the slope at the end of the plateau and during the repolarization, we hypothesized that further heterogeneities should be included in the *in silico* experiments, in particular in the AP amplitude and in the plateau phase.

2.2.3. Transmembrane potential rescaling

According to the experimental measurements of Fig. 5, the interval between depolarization and repolarization is almost never flat and varies a lot among the different signals. We noticed that this behavior could be reproduced by creating a difference in the peak and in the plateau phase of the APs in different parts of the monolayer of cells. We rescale the transmembrane potential V_M : this way a gradient is encountered by the electrotonic current. The study by the Antzelevitch group [4] shows that the amplitude of the AP can vary from the registered mean value. The standard deviation of this variation is around 25% of the mean value of the amplitude in each

phenotype. We include this experimental evidence in the model by rescaling the transmembrane potential V_M in one or more parts of the domain Ω . Because of the absence of a detailed description of how the different cell phenotypes are distributed in the experiment, we try different repartitions. To understand the effect of the heterogeneities in that AP magnitude, we start with a simple splitting of the domain. As shown in Fig. 6, our goal is to simulate an action potential with a sufficiently high spatial gradient at the plateau phase, allowing to reproduce FPs with the same shape as the experimental signals. If we denote by V_{rest} the resting potential of the Paci model and take $0 < c_1 < 1$ and $c_2 = (1 - c_1)V_{rest}$, by solving the following zero-D models

$$\begin{cases} A_M \left(C_M \frac{dV_1}{dt} + I_{ion}(V_1, \mathbf{w}_1, t) \right) = 0 \\ \frac{d\mathbf{w}_1}{dt} = \mathbf{g}(V_1, \mathbf{w}_1, t), \end{cases} \quad (4)$$

$$\begin{cases} A_M \left(C_M \frac{dV_2}{dt} + c_1 I_{ion} \left(\frac{1}{c_1}(V_2 + c_2), \mathbf{w}_2, t \right) \right) = 0 \\ \frac{d\mathbf{w}_2}{dt} = \mathbf{g} \left(\frac{1}{c_1}(V_2 + c_2), \mathbf{w}_2, t \right). \end{cases} \quad (5)$$

we obtain

$$V_2 = c_1 V_1 - c_2 \text{ and } \mathbf{w}_1 = \mathbf{w}_2. \quad (6)$$

Since the standard deviation of the action potential magnitude variation is around 25% of the mean value of the amplitude in each phenotype [4], in what follows we will take $0.7 \leq c_1 \leq 1$. By splitting the domain Ω into two regions Ω_1 and Ω_2 as described in Fig. 6, we introduce the rescaling heterogeneity in the bidomain model as follows

$$\begin{cases} A_M \left(C_M \frac{\partial V_M}{\partial t} + I_{ion}(V_M, \mathbf{w}_1, t) \right) - \text{div}(\sigma_I \nabla (V_M - u_e)) = A_M I_{stim} \text{ in } \Omega_1 \\ \frac{d\mathbf{w}_1}{dt} = \mathbf{g}(V_M, \mathbf{w}_1, t) \quad \text{in } \Omega_1 \\ A_M \left(C_M \frac{\partial V_M}{\partial t} + c_1 I_{ion} \left(\frac{1}{c_1}(V_M + c_2), \mathbf{w}_2, t \right) \right) - \text{div}(\sigma_I \nabla (V_M - u_e)) = A_M I_{stim} \text{ in } \Omega_2 \\ \frac{d\mathbf{w}_2}{dt} = \mathbf{g} \left(\frac{1}{c_1}(V_M + c_2), \mathbf{w}_2, t \right) \quad \text{in } \Omega_2. \end{cases} \quad (7)$$

Equations (1a) and (1c) are replaced by the systems of equations (7). The electrotonic current introduced by the diffusion terms will avoid the discontinuity in the transmembrane potential at the interface between Ω_1 and Ω_2 .

2.2.4. Arrangement in clusters

The splitting in two domains presented in Fig. 6 is clearly arbitrary. Here we consider other kinds of cell arrangements giving results which are also in good qualitative agreement with the experiments. The underlying idea is to generate many different plausible configurations from which it will be possible to do statistics. This strategy allows us to limit the impact of arbitrary choices of cells distribution and can be a good way to circumvent the absence of information about the cell variability and heterogeneity in each well. A 10×10 grid of squares $(\omega_i)_{i=1,\dots,100}$ is introduced in Ω . Let \mathcal{I}_1 and \mathcal{I}_2 be a partition of the set $\{1, \dots, 100\}$. Each ω_i is assigned to one of the two subdomains introduced in Eq. (6): $\Omega_1 := \cup_{i \in \mathcal{I}_1} \omega_i$ and $\Omega_2 := \cup_{i \in \mathcal{I}_2} \omega_i$. Let F be the fraction of domain Ω where the rescaling is employed, namely $F := |\Omega_2|/|\Omega|$ ($|\cdot|$ stands for the surface measure). We keep $F = 20\%$ and we randomly change the spatial arrangement of Ω_1 and Ω_2 for every simulation. Two classes of configuration are considered: the “*clustered*” configurations, when Ω_2 is a big connected part, and the “*scattered*” configurations, when Ω_2 is scattered into multiple small subdomains. Examples of such configurations are given in Fig. 11.

2.2.5. Reproducing the field potential variability

Given the variability observed in the experiments (see e.g. the measurements for 6 different wells in Fig. 5(a)) and the uncertainties of the model, the exact *in silico* reproduction of a specific experiment would not make much sense. Instead, we propose to consider several scenarios and compute averages and standard deviations of quantities of interest. We indicate in this section how the scenarios are elaborated. In the subsections 2.2.2 and 2.2.3, two ways of reproducing the shape heterogeneity of the signals measured from hiPSC-CMs preparations have been investigated: the introduction of two phenotypes (atrial and ventricular types) and the introduction of a rescaling in the AP amplitude. We will use these two tools to generate various configurations. To do so, the domain is split as $\Omega = \Omega_1 \cup \Omega_2$ and we consider in Ω_1 a ventricular model with a rescaling while in Ω_2 we consider an atrial model. The splitting is performed by favoring clustered configura-

tions. The ventricular-like transmembrane potential is rescaled because the AP amplitude of ventricular cells is lower, in average, than the one of atrial cells [4]. Following the experimental results in [4] and taking to account the maturity and phenotype heterogeneities, we set the parameters c_1 and c_2 in order to reduce the magnitude of the AP by about 30% in Ω_2 .

2.3. Model for the drug/ion channels interactions

The *in silico* approach presented in the previous sections was designed to qualitatively mimic the field potential acquired with MEA measurements (see Fig. 13), by taking into account a certain amount of variability. Our purpose is now to introduce in the model the action of compounds on ion channels. The modeling of drug-channel interactions has been the object of several studies (see e.g. [16, 27]). Various concepts have been introduced 1) *pore block* action: the flow of ions is inhibited by the drug binding with a continuously accessible channel receptor; 2) *modulated and guarded receptor* theories: the drug access to the binding sites is restricted due to the channel conformation during the AP cycle; 3) *allosteric effectors*: a drug binding to a protein changes its activity and also activates conformational changes in its dynamics. In the present study, the pore block model is used because it does not require too many parameters and because it proved to be able to reproduce the relevant phenomena. The pore block model is implemented with the “conductance-block” formulation [28, 29, 15, 30]. The conductance of the targeted channel is reduced by a scaling factor in the following way:

$$g_s = g_{control,s} \left[1 + \left(\frac{[D]}{IC_{50}} \right)^n \right]^{-1}, \quad (8)$$

where $g_{control,s}$ is the drug-free maximal conductance of channel s , the IC_{50} value of the drug is the drug concentration at which a 50% reduction of the specific channel peak current is observed and $[D]$ is the drug concentration. The Hill coefficient n will be assumed to be equal to 1.

3. Results

In this section, we first present the MEA signals given by our simulation and the impact of the modeling choices presented in subsection 2.2 to handle heterogeneity and variability. Next, in the second part of this section, we investigate the influence of drugs on numerical MEA signals and compare

them to experimental data. All *in silico* and *in vitro* signals that will be presented below are obtained without introducing any stimulation current. The firing occurs because of the pacemaker behavior of the cells, *in vitro* and *in silico*.

3.1. MEA signals simulation

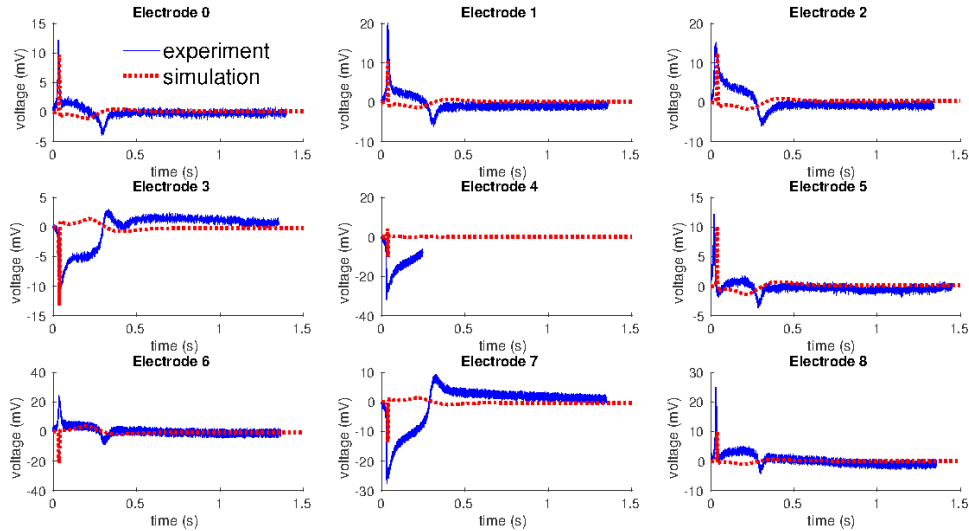


Figure 7: Field potentials measured by the 9 electrodes: comparison between experimental and simulation signals, obtained with the phenotype heterogeneity model.

To start with, we consider an heterogeneous media with two different phenotypes as explained in Section 2.2.2. In Fig. 7, the results provided by our model (red lines) can be compared with experimental signals (blue lines). We observe that the depolarization is sharper in the simulations than in the experiments and that the shapes of the FP during the plateau phase exhibit significant differences. This motivates the use of the rescaling strategy, presented in Section 2.2.3. The results obtained with the rescaling are compared with the experimental measurements in Fig. 8. The simulation results (red lines) are now closer to the measured signals (blue lines). Even if polarity differences remain for some electrodes, the agreement is very good for electrodes 1, 2, 3 and 5. Globally, a comparison with Fig. 7 shows that the experimental measurements are better reproduced in the present case, especially in the depolarization and in the plateau phases.

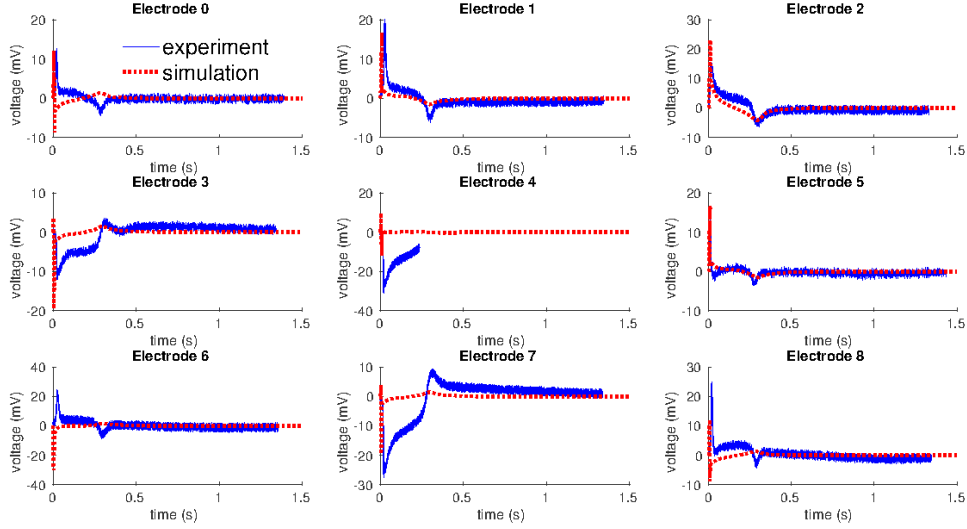


Figure 8: Field potentials measured by the 9 electrodes: comparison between experimental and simulation signals, obtained with the transmembrane rescaling model (all cells are ventricular-like).

In Fig. 9(b) we present the simulated FP signals obtained with the rescaling procedure, which can be compared to those obtained without the rescaling procedure (Fig. 3). In Fig. 9(a), we show the corresponding action potential (AP) traces averaged over the electrodes. One could see that the magnitude of the transmembrane potential in the plateau phase is gradually rescaled from the left bottom to the right top corner. This gradation is due to the electrotonic effect. In Fig. 9(d) (respectively, Fig. 9(c)), we present the simulated FPs (respectively, APs) obtained when introducing only a phenotype heterogeneity. The repartition of cells phenotypes follows the example in Fig. 6, where in Ω_1 we use ventricular model and in the domain Ω_2 , we use atrial cells model. One could see in Fig. 9(c) a gradation in the AP duration from the top right representing atrial phenotype to the bottom left corners representing ventricular phenotype. Also this result can be explained by the electrotonic effect. We observe that the rescaling allows to have numerical results closer to the experimental curves presented in Fig. 4. The level of heterogeneity is then quantified in the box plots presented of Fig. 10: the magnitudes of the repolarization peak (Fig. 10(a)) and of the depolarization-repolarization interval (Fig. 10(b)) show a significantly higher standard deviation when the rescaling strategy is introduced in the model.

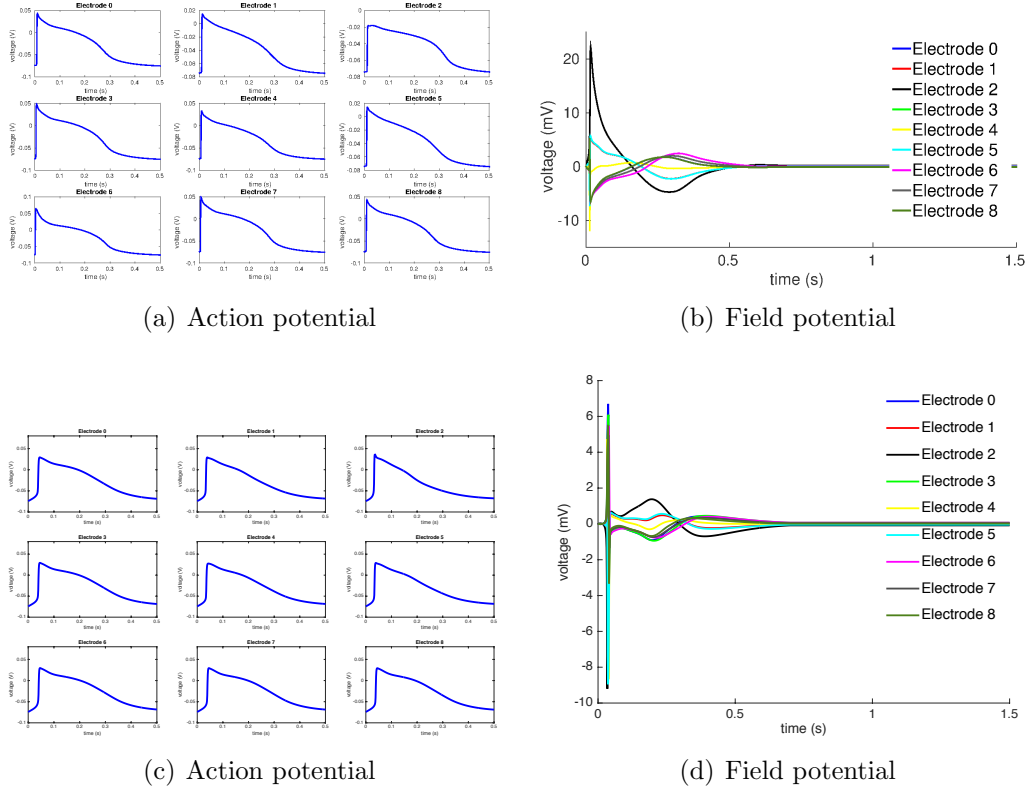


Figure 9: Simulated transmembrane and field potentials over the 9 electrodes for ventricular-like hiPSC-CMs with the rescaling procedure presented in Section 2.2.3 (top). Simulated transmembrane and field potentials over the 9 electrodes using phenotype heterogeneity (bottom).

In the absence of rescaling (Fig. 3) the tissue is stimulated at the bottom-left corner with $I_{stim} = 150 \mu\text{A cm}^{-2}$ for 1 ms to trigger the propagation. In all these simulation, we have considered a clustered configuration (as introduced in Section 2.2.4). Let us now compare the results obtained with the clustered and scattered repartitions of cells. In Fig. 11 and Fig. 12, a comparison of the results obtained with these two arrangements is shown: the clustered configuration produces a higher level of variability of the FP shapes and of the repolarization magnitude than the scattered one. This last configuration tends to flatten the effects of heterogeneity. These results are in agreement with experimental observations, since the differentiation between cells is distributed in a sort of clustered manner and also neighbour-

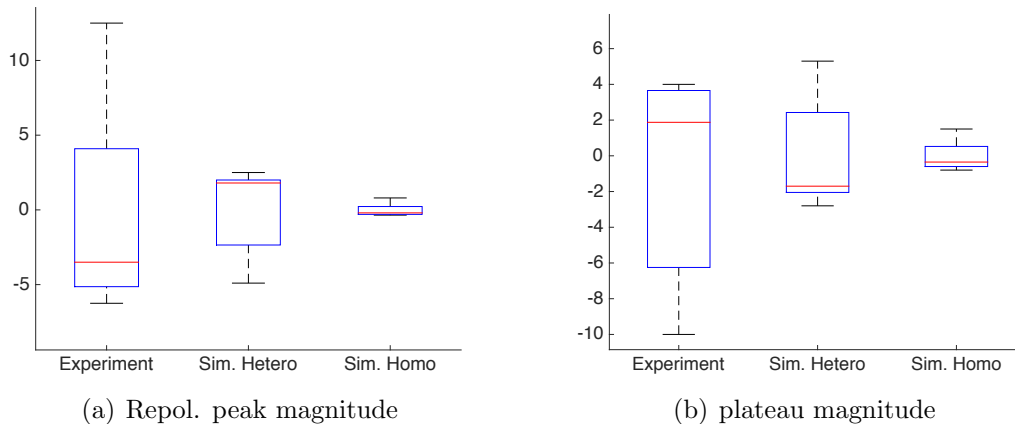


Figure 10: Effect of the rescaling heterogeneity on the plateau and repolarisation peak amplitudes of the field potential: Experimental data (first box), simulation with heterogeneity (second box) and simulation without heterogeneity (third box). Y-axis refers to voltage, values are in mV.

ing cells have influence on each other [6]. Finally, to mimic the variability observed in the experiments and to generate several scenarios, we follow the strategy explained in Section 2.2.5 which mixes the two previous approaches by introducing two phenotypes and differences in the AP amplitude. Six different configurations are implemented by changing the ratio and the spatial arrangement of the subdomains Ω_1 and Ω_2 . This allows to generate 54 signals that will be used for the statistics in the next subsection. In Fig. 13, the results obtained with this procedure are shown. A visual inspection shows that the experimental variability of amplitude, frequency, shape and duration of the signals seems to be qualitatively well reproduced by these computations. In all the simulations where heterogeneities are introduced (by phenotype or by AP rescaling), we did not introduce any stimulation.

3.2. Assessment of the *hiPSC-CMs/MEA/Drug* model

In this section, results for different compounds are presented, commented and compared with experimental observations. The experiments are performed with a 6-well MEA, all data are provided by Janssen Pharmaceuticals, Inc., and post-processed by Notocord[®]. A set of 54 *in silico* signals is generated as explained right above in order to compute some statistics and to assess that the general effects of the specific drug are well reproduced by the model. In the experimental data, we select from the 54 experimental

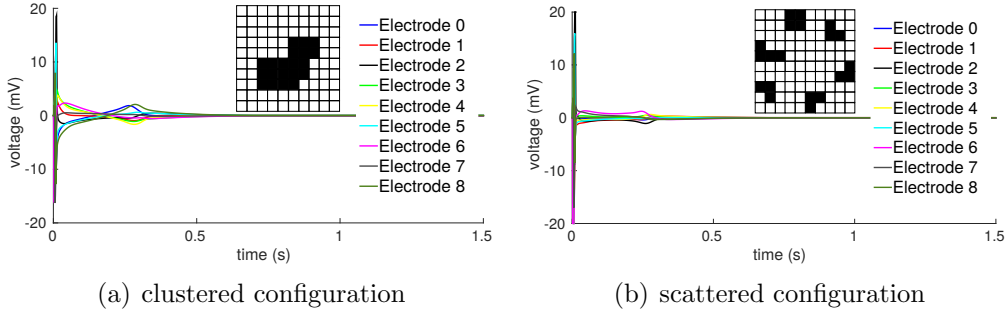


Figure 11: Field potential shapes obtained with $F = 20\%$, with two different spatial arrangements (the black part is Ω_2): on the left results for a “clustered configuration”, on the right results for a “scattered configuration”.

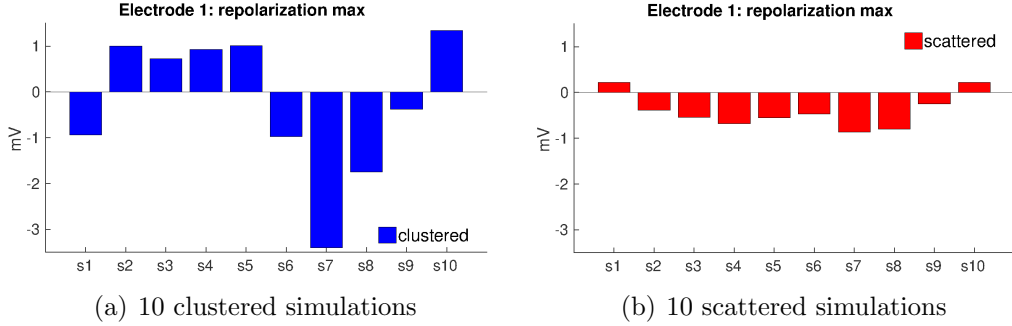


Figure 12: Repolarization magnitudes of the field potential collected by a single electrode for 10 clustered simulations (left) and 10 scattered simulations (right). All results obtained with $F = 20\%$.

signals those which are clean enough for extracting the different biomarkers. For the sake of clarity, the measurements and the simulations are presented for only one electrode. Figures containing the traces of the field potential for the 9 electrodes with multiple heart beats for both *in vitro* and *in silico* experiments are provided in the supplementary material.

3.2.1. Mexiletine

The effects of mexiletine on hiPSC-CMs are the blocks of the sodium and of the L-type calcium currents with $IC_{50, I_{Na}} = 106.25\mu\text{M}$ and $IC_{50, I_{CaL}} = 75\mu\text{M}$ [31]. Therefore this compound has an impact mainly on the depolarizing phase of cells, as can be observed in the measurements of Fig. 14(a). The same dose-dependent effects are observed in both experiments and sim-

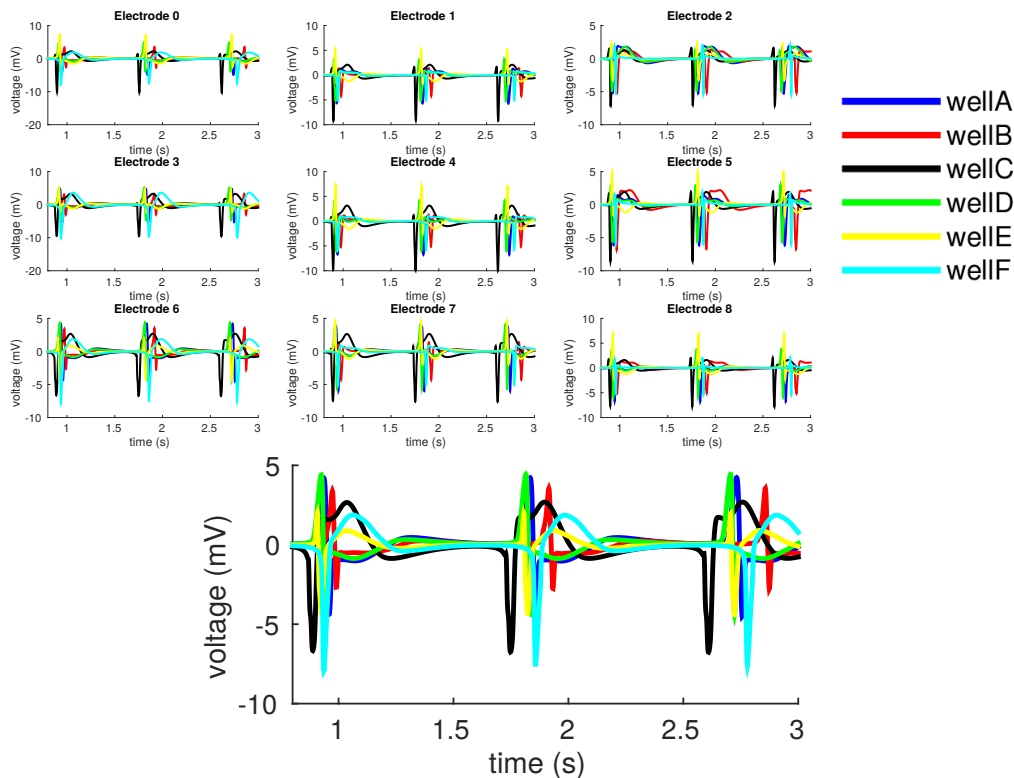


Figure 13: Field potentials obtained with the phenotype heterogeneity model together with the rescaling of the ventricular-like V_M . 6 heterogeneity cases: change of the domain splitting and of the rescaling parameters c_1 and c_2 inside the physiological range.

ulations (see the comparison of one beat in Fig. 14: blue lines correspond to control conditions, red lines to $50\mu\text{M}$ and black lines to $100\mu\text{M}$). The reduction of the depolarization amplitude is well reproduced. The results obtained with a simulation of 4s are shown in Fig. 15. These curves correspond to one electrode and one configuration of cells. The frequency of firing is consistently reduced in presence of mexiletine. The same effect was observed in all the other studied configurations. In the paper by Harris *et al.* [9], it is observed that the beating is stopped in 3 out of 5 plates, with $30\mu\text{M}$ of mexiletine. Nevertheless, the present experimental data do not show this behavior. In order to get a more general assessment, we have reported in Table 2(a)-(b) the mean and standard deviation of the effect on the depolarization for six simulated wells (54 signals) and for the six experimental wells.

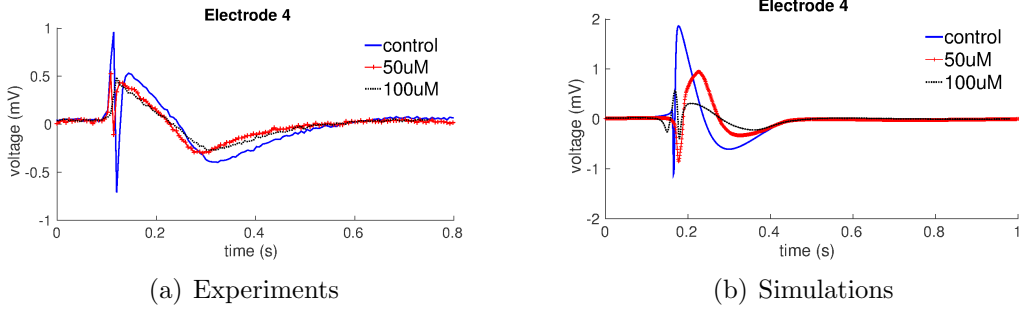


Figure 14: Comparison of the field potential between control conditions and 50µM and 100µM of mexiletine for one beat: experimental measurements (a) and simulations results (b).

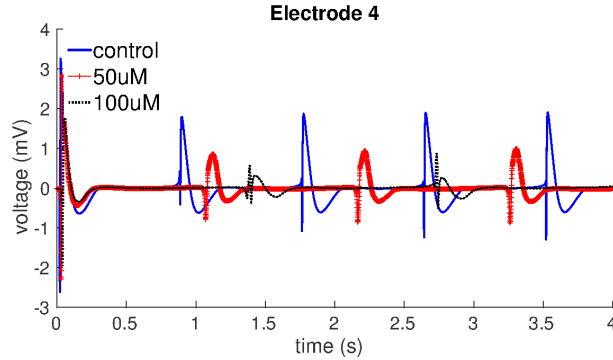


Figure 15: Comparison of the field potential between control conditions and 50µM and 100µM of mexiletine for 4 seconds simulation.

For the experimental signals, a few electrodes with a too low signal to noise ratio were removed. The amplitude of the depolarization wave is computed as the absolute difference between the maximum and the minimum of the FP during depolarization. The relative depolarization amplitude (amplitude of the signal with the drug relative to the amplitude in control conditions) is computed as

$$\text{RelAmpl}_{i,j} = \frac{\text{Ampl}_{dose}^{i,j}}{\text{Ampl}_{control}^{i,j}} \quad \text{for } i = i^{th} \text{ well, } j = j^{th} \text{ electrode.} \quad (9)$$

This is a quantification of which fraction of the “control amplitude” is obtained with a certain dose. The mean values of our simulations confirm that the general effect of mexiletine is well reproduced: the higher the drug

concentration the smaller the absolute and relative amplitudes. The statis-

(a) Experiments			(b) Simulations		
Depol. ampl	Mean	Std dev	Depol. ampl	Mean	Std dev
Control	1.7425	0.6374	Control	8.6241	2.0071
50 μ M mex	1.2104	0.6698	50 μ M mex	3.8681	1.0106
100 μ M mex	0.7228	0.3438	100 μ M mex	2.8364	0.9758
Depol. relative ampl			Depol. relative ampl		
50 μ M mex	0.6841	0.2223	50 μ M mex	0.4525	0.0795
100 μ M mex	0.4392	0.1729	100 μ M mex	0.3300	0.0800

(c) Experiments			(d) Simulations		
Repol. peak	Mean	SD	Repol. peak.	Mean	SD
Control	0.1980	0.26	Control	0.36	0.1031
50 μ M mex	0.1800	0.24	50 μ M mex	0.26	0.1129
100 μ M mex	0.1380	0.15	100 μ M mex	0.1780	0.1234
Repol. peak rel. amp.	Mean	SD	Repol. peak rel. amp.	Mean	SD
50 μ M mex	0.8239	0.2960	50 μ M mex	0.6988	0.1652
100 μ M mex	0.6293	0.3605	100 μ M mex	0.4922	0.1774

Table 2: Statistics computed on simulated and experimental signals to assess the effect of mexiletine. Absolute values of mean and standard deviation of the depolarization amplitude and repolarization peak amplitude in control conditions and with 50 μ M and 100 μ M.

tics results on simulations and on experiments are comparable, especially the relative ones. The difference in control conditions between simulations (8.6241 ± 2.0071) and experiments (1.7425 ± 0.6374) might be due to an imperfect modeling of the electrodes. But rather than an absolute value, the important information is that the general trend is well captured by the model. In Table 2(c)-(d), we compare the statistics on the repolarization peak amplitude of experimental and simulated signals: a reduction is observed in both *in vitro* and *in silico*, but more pronounced in the latter. Regarding the repolarization time, we report in Table 3.2.1 (a)-(b) statistics on the repolarization time (RT) with and without rate correction. Corrections follow Bazett’s formula. We observe that, without rate correction RT intervals are increase when introducing each drug dose. But in experiment, this effect is more pronounced with 50 μ M than with 100 μ M, which is not the case in the *in silico* simulations. When looking at the rate corrected repolarization times, we observe the same effect as without rate correction in the experimental data. But in the *in silico* results, we observe that the rate corrected RTs decrease with respect to the drug dose.

(a) Experiments			(b) Simulations		
RT	Mean	SD	RT	Mean	SD
Control	0.1714	0.0242	Control	0.3403	0.0276
50μM mex	0.2096	0.0291	50μM mex	0.3555	0.0276
100μM mex	0.1826	0.0123	100μM mex	0.3965	0.0321
RT (rate corrected).	Mean	SD	RT (rate corrected).	Mean	SD
Control	0.1768	0.0232	Control	0.3582	0.0238
50μM mex	0.2350	0.0359	50μM mex	0.3295	0.0224
100μM mex	0.2053	0.0101	100μM mex	0.3222	0.0256

Table 3: Statistics computed on simulated and experimental signals to assess the effect of mexiletine. Repolarization time with and without rate correction in control conditions and for 50μM and 100μM drug doses.

3.2.2. Dofetilide

Dofetilide is known to block the I_{Kr} channel with $IC_{50, I_{Kr}} = 5\text{nM}$ [29]. This induces a delay and a reduction of the peak amplitude in the repolarization phase. In Fig. 16, blue lines correspond to control conditions, red lines to 10nM and black lines to 50nM. In both experimental and simulation curves, we can notice the same dose-dependent delay of the repolarization wave and also a (slight) reduction of the peak amplitude of the repolarization.

In Table 4(c)-(d), we show the effect on the FP repolarization for different heterogeneity configurations. The reduction of the repolarization maximal amplitude (absolute values and values relative to control conditions) shows very high standard deviations. It is therefore difficult to draw a conclusion on this aspect. The delay of repolarization for a given dose is quantified as the difference between the instant of the repolarization peak in presence and absence of dofetilide:

$$\text{TDelay}_{i,j} = \text{time}_{\text{repol,dose}}^{i,j} - \text{time}_{\text{repol,control}}^{i,j} \quad \text{for } i = i^{\text{th}} \text{ well, } j = j^{\text{th}} \text{ electrode.} \quad (10)$$

We compute the rate correction of the time delay TDelay^c using Bazett's formula as follows

$$\text{TDelay}_{i,j}^c = \frac{\text{time}_{\text{repol,dose}}^{i,j}}{\sqrt{RR_{\text{dose}}^{i,j}}} - \frac{\text{time}_{\text{repol,control}}^{i,j}}{\sqrt{RR_{\text{control}}^{i,j}}}, \quad \text{for } i = i^{\text{th}} \text{ well, } j = j^{\text{th}} \text{ electrode.} \quad (11)$$

This delay, causing an increase of the signal duration, is well reproduced in all our simulations, as confirmed by the computed statistics in Table 4(e). Repolarization delay statistics in the experimental data are reported in Table

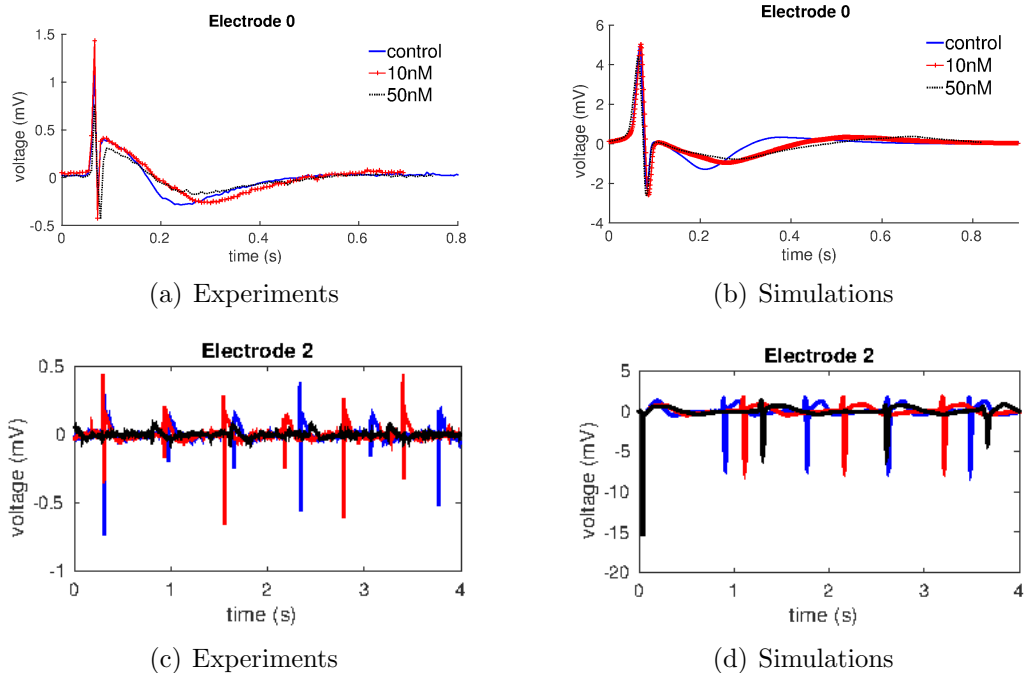


Figure 16: Comparison between control conditions and 10nM and 50nM of dofetilide for one beat: experimental measurements (a) and simulations results (b).

4(f). We observe that the delay periods with and without rate correction are less pronounced in the experimental data than they are in the *in silico* results.

In Figure 16(c) and 16(d), we show multiple beats: one could see that dofetilide reduces the spike amplitude. This effect is clearly seen in *in vitro* experiments, as shown also by Table 4(a). The same effect is present also *in silico*, but it is less pronounced. As a consequence, we also see that dofetilide reduces beating rate of the stem cells. In fact, the cycle length in the simulated results is 0.903 ± 0.028 s (respectively, 1.114 ± 0.043 s, 1.349 ± 0.037 s) for the control (respectively, 10nM, 50nM) case. These unexpected effects have been reported in the case of *in vitro* experiments in the work by Qu and Vargas (2015) [32]. More figures on the effect of dofetilide on the nine electrodes extracted from one well are provided in the supplementary material.

3.2.3. BayK

Bay K8644 is an I_{CaL} agonist, namely a drug that activates the L-type calcium channels by increasing the current in a dose-dependent manner. This

(a) Experiments			(b) Simulations		
Depol. rel. amp.	Mean	SD	Depol. rel. amp.	Mean	SD
10nM dofetilide	0.817	0.198	10nM dofetilide	1.016	0.10
50nM dofetilide	0.389	0.219	50nM dofetilide	0.949	0.119

(c) Experiments			(d) Simulations		
Repol. peak amplitude	Mean	SD	Repol. peak amplitude	Mean	SD
Control	0.0986	0.1143	Control	0.3631	0.2601
10nM dofetilide	0.0906	0.1066	10nM dofetilide	0.3272	0.2224
50nM dofetilide	0.0644	0.0733	50nM dofetilide	0.3223	0.2341
Repol. peak rel amp.	Mean	SD	Repol. peak rel amp.	Mean	SD
10nM dofetilide	0.9367	0.1083	10nM dofetilide	0.9048	0.0848
50nM dofetilide	0.8495	0.1642	50nM dofetilide	0.7089	0.1701

(e) Simulations				
Repol. wave time delay	Mean	SD	Mean (rate corrected)	SD (rate corrected)
10nM dofetilide	0.1579	0.0822	0.1311	0.0848
50nM dofetilide	0.2863	0.0897	0.2126	0.0844

(f) Experiment				
Repol. wave time delay	Mean	SD	Mean (rate corrected)	SD (rate corrected)
10nM dofetilide	0.043	0.035	0.068	0.048
50nM dofetilide	0.081	0.057	0.055	0.024

Table 4: Comparison of the effect of dofetilide on the field potential for both in silico and in vitro experiments. The comparison is evaluated on repolarization peak amplitude, depolarization amplitude and repolarization wave delay for doses 10 nM and 50 nM.

action evidently cannot be modeled with the conductance block formulation, because the conductance needs to be increased. The following relation models the effect of an agonist on a generic channel s [33]:

$$g_s^A = g_s \left(1 + \frac{\alpha D^n}{K_A^n + D^n} \right). \quad (12)$$

g_s^A is the conductance modified with the agonist, depending on the conductance in control conditions g_s , on the drug dose D , on the Hill coefficient n , on α (the maximal relative increase of the channel current induced by the agonist) and on the dissociation constant K_A . In Fig. 17, both the experimental and the simulation signals clearly show the expected prolongation of the plateau when BayK is added. The two doses of 1 μ M and 5 μ M produce almost the same effect (signals almost superposed), because they are close to the threshold of concentration after which the effect is at its maximum. This behavior is present in both experiments and simulations. The general effect

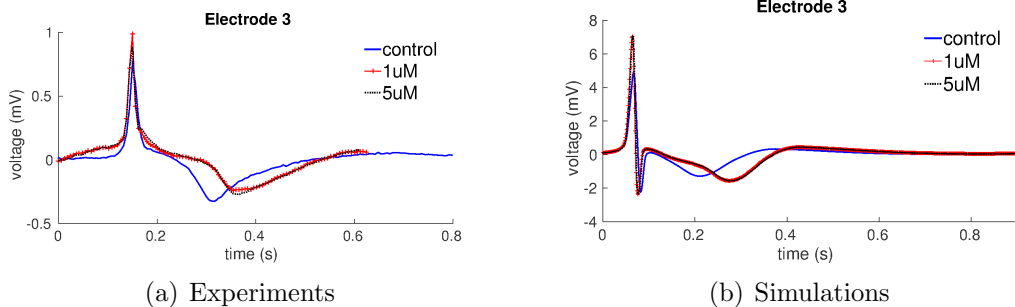


Figure 17: Comparison between control conditions and 1µM and 5µM of BayK for one beat: experimental measurements and simulations results.

is always reproduced, as observed when running simulations for six different configurations. The plateau duration can be quantified as

$$P_{duration}^{i,j} = t_S^{i,j} - t_{repol}^{i,j} \quad \text{for } i = i^{th} \text{ well, } j = j^{th} \text{ electrode,} \quad (13)$$

$t_S^{i,j}$ being the time of the end of the depolarization and t_{repol} the peak of the repolarization time. Table 5(a) (respectively, (b)) shows the mean values and the standard deviations of the plateau duration for the in silico (respectively, in vitro) signals for each drug dose. We observe that when adding BayK, the mean value increases dose-dependently. For the two doses, the mean values are very close for the reason explained above when commenting the superposed curved of Fig. 17. In Table 5(c)-(d) the effect of BayK on the T-peak magnitude is presented. We observe that this biomarker is decreased in the experimental data, whereas it is increased in simulation: for a dose of 5µM, the mean of the relative magnitude of the T-peak is 0.76 in experiments and 1.34 in simulations.

3.2.4. Ivabradine

Ivabradine is a compound which blocks the funny current I_f with $IC_{50} = 2.1\mu\text{M}$ [34]. I_f is only present in pacemaker cells and is able to give rise to instability during the resting potential phase. Therefore, the general effect of ivabradine is a decrease of the beating frequency, which can be observed on the measurements plotted in Fig. 18(a). In Fig. 18(b), the simulations results obtained with a specific configuration on one electrode are shown. In both experimental and computed signals, the frequency is slowed down as the concentration of ivabradine is increased. The drug does not alter the general

(a) Simulations

Plateau duration	Mean	SD	Mean (rate corrected)	SD (rate corrected)
Control	0.1166	0.0583	0.1240	0.062
1 μ M BayK	0.1770	0.0609	0.1844	0.0634
5 μ M BayK	0.1802	0.0609	0.1858	0.0628

(b) Experiment

Plateau duration	Mean	SD	Mean (rate corrected)	SD (rate corrected)
Control	0.1513	0.0152	0.1106	0.0724
1 μ M BayK	0.1702	0.0264	0.2419	0.0387
5 μ M BayK	0.1855	0.0146	0.2616	0.0226

(c) Experiments

(d) Simulations

Repol. peak amplitude	Mean	SD	Repol. peak amp.	Mean	SD
Control	0.3675	0.2193	Control	0.4373	0.1711
1 μ M BayK	0.3100	0.1977	1 μ M BayK	0.5775	0.1979
5 μ M BayK	0.2963	0.2186	5 μ M BayK	0.5777	0.1976
Repol. peak rel amp.	Mean	SD	Repol. peak rel. amp.	Mean	SD
1 μ M BayK	0.8315	0.0815	1 μ M BayK	1.3489	0.1678
5 μ M BayK	0.7670	0.1031	5 μ M BayK	1.3499	0.1684

Table 5: Comparison of the effect of BayK on the field potential for both *in silico* and *in vitro* experiments. The comparison is evaluated on repolarization peak amplitude and on the plateau duration for doses 1 μ M and 5 μ M.

shape of the FP. In all the studied configurations, the computational model gives the expected effects, even though the delay is lower than in experiments. In Fig. 19(a) (respectively, (b)), we show how ivabradine prolongs the cycle length in the experimental (respectively, simulated) case. We see that the effect is much more pronounced in the experiments than it is in the *in silico* model.

3.2.5. Bepridil

As a last example, we reproduce the effects of bepridil, a compound that blocks multiple channels. The main action is on I_{Kr} , but for high doses it also affects the sodium channel I_{Na} and the L-type calcium current I_{CaL} : the IC_{50} values for the three channels are respectively 33nM, 3.7 μ M and 211nM [29]. In Fig. 20, the doses of 1 μ M and 5 μ M are analyzed: at these concentrations, all the three channels are affected and the whole signal is dose-dependently changing. In our results in Fig. 20(b), the repolarization wave almost disappears, the depolarization is enlarged and its amplitude decreases with the drug dose. The duration is slightly increased due to the fact that bepridil affects more I_{Kr} than I_{CaL} . The same effects are also present in the experimental signals of Fig. 20(a), but less pronounced: the

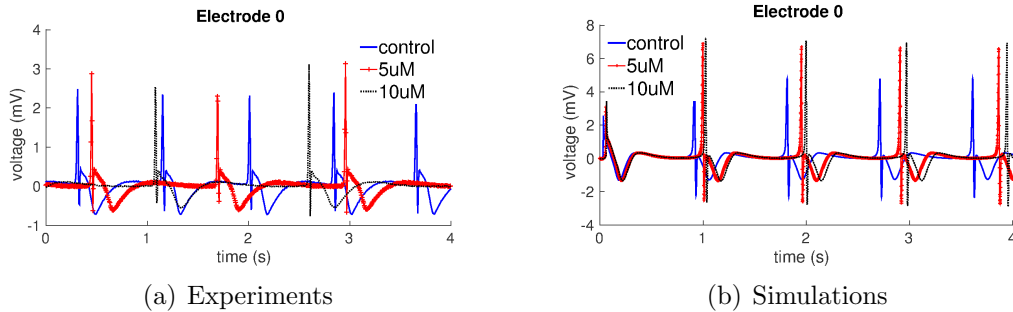


Figure 18: Comparison between control conditions and 5 μ M and 10 μ M of ivabradine for 4 seconds: experimental measurements and simulations results.

amplitude of the depolarization is reduced but the wave is not enlarged and the peak of the repolarization is delayed but does not disappear. This can be explained by the fact that the IC_{50} values that we are using are not fitted on the case of hiPSC-CMs but on guinea pig CMs. In the case of stem cells, for bepridil, we expect that higher IC_{50} values would better reproduce the experimental signals. In Table 6, we quantify the action of bepridil on the

(a) Experiments			(b) Simulations		
Depol. ampl	Mean	Std dev	Depol. ampl	Mean	Std dev
Control	1.9663	1.0452	Control	8.6241	2.0071
1 μ M	1.6432	0.7428	1 μ M bep	2.8250	1.0764
5 μ M	1.2977	0.6707	5 μ M bep	1.3844	0.5712
Depol. relative ampl			Depol. relative ampl		
1 μ M	0.8771	0.2223	1 μ M bep	0.3337	0.0962
5 μ M	0.6952	0.3200	5 μ M bep	0.1599	0.0495

Table 6: Statistics computed on simulated and experimental signals to assess the effect of bepridil. Absolute values of mean and standard deviation of the depolarization amplitude in control conditions and with a dose of 1 μ M and 5 μ M. Relative values computed as in relation (9).

depolarization wave for the six simulations cases and the six wells, as done for the case of mexiletine. The mean values confirm that the reduction of the depolarization amplitude is reproduced by the simulations. Regarding the experimental measurements, the standard deviations are very high, because this set of data are noisy. As observed above, the computation results show a more pronounced effect of the compound than the experiments.

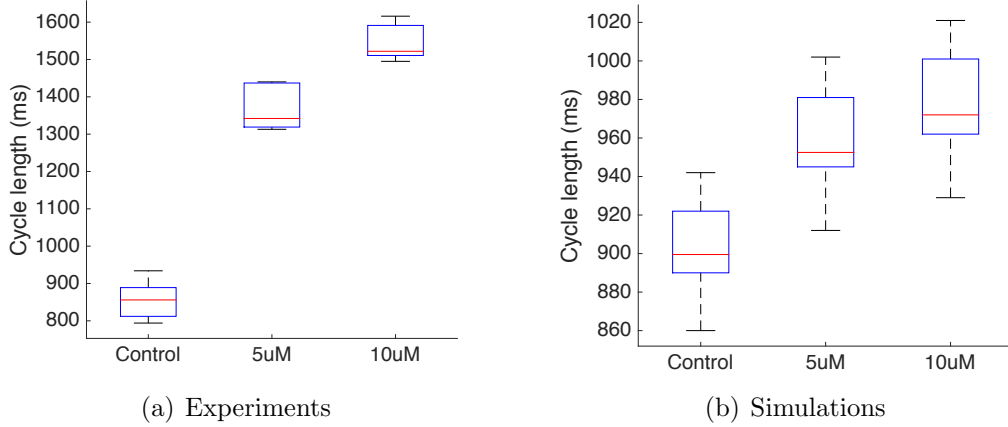


Figure 19: Effect of Ivabradine on the activation rate: Comparison between control conditions and 5 μ M and 10 μ M, experimental measurements (left) and simulations results (right).

4. Discussion and conclusion

The main objective of the study was to introduce a mathematical model of MEA measurements on hiPSC-CMs. After its mathematical derivation, the model has been tested with several simulations and compared with experimental measurements. Many modelling hypotheses were justified by literature studies and experimental observations. Based on the works [6, 9, 4, 5], two different phenotypes have been introduced in the model and a variability in the action potential amplitudes has been taken into account. We do not have any information on how the cells are seeded in the monolayer preparation. According to the collected signals and to the simulation obtained with the mathematical model that we use, our hypothesis is that phenotypes are organized in a clustered manner.

Obtaining *in silico* signals that exactly match a specific experiment is very difficult and not necessarily desirable. The difficulty comes from various experimental uncertainties. However, the model was able to qualitatively reproduce the main features observed in the experiments. This proved to be sufficient to detect the effect of drugs, which were studied with the pore block model. MEA pharmaceutical experiments were simulated for five different compounds. Again, the assessment was not done by a point to point comparison, which would not make sense given the variability of the experiments.

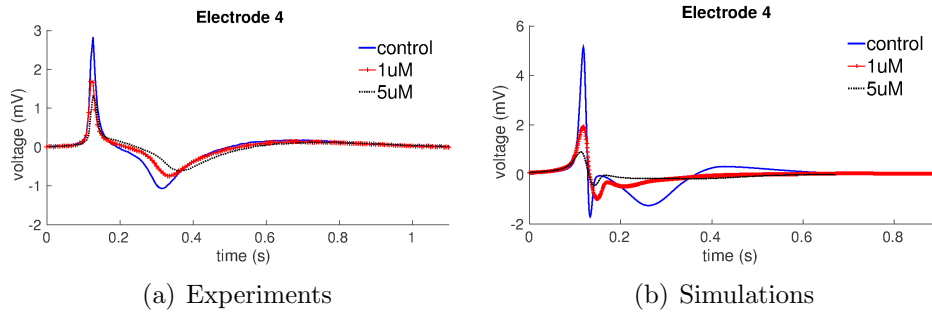


Figure 20: Comparison between control conditions and 1 μ M and 5 μ M of bepridil for one beat: experimental measurements and simulations results.

Instead, it was performed by considering average trends of biomarkers. For Mexiletine, our study shows a good agreement in terms of depolarization and repolarization peak amplitudes between *in vitro* and *in silico* results. On the contrary, the comparison on the repolarization times shows that the effect of Mexiletine of the RT without rate correction is not monotonous with the value of the drug dose in the *in vitro* measurements, whereas it is in the *in silico* data. However, when introducing rate correction we obtain this non-monotonicity for both *in silico* *in vitro* signals, but still more pronounced in experiments than it is in simulations. For dofetilide, both *in silico* and *in vitro* models show a repolarization delay and a reduction of the repolarization peak amplitude with the drug doses. However, the effect of dofetilide on the depolarization amplitude was very small in simulation compared to what it is in experiments. A high effect of dofetilide on the depolarization is not expected because it is not supposed to affect the sodium current. This unexpected effect has been reported in the experimental study by Qu and Vargas (2015) [32] where for high doses of dofetilide early after depolarization waves appear and may consequently alter the sodium current in the depolarization. This could explain the reduction of the depolarization wave magnitude. More investigations on both *in vitro* and *in silico* experiments are needed in order to clarify this issue. For BayK, we obtained a good agreement between simulation and experiment in terms of repolarization delay due to an increase of the plateau duration. However, both models provide do not agree on the effect of BayK on the depolarization magnitude. While in experiments we observe a decrease of this biomarker, in the simulation we observe a pronounced increase of the depolarization magnitude with the drug dose. The reason of

this contradictory effect is not clear, it could be related to the formulation of the calcium current in the Paci et al [18] model. Again more investigations are needed in order to elucidate this question. For bepridil, both models are in agreement in the effect of the drug on the reduction of depolarization amplitude which is more pronounced in the *in silico* model. For Ivabradine both models are also in agreement its effect on prolonging cycle length with a higher effect in the *in vitro* model. Even if for some compounds the effect was more pronounced in the simulations than in the experiments, the *in silico* model generally gave results in good agreement with the experiments. Many aspects of the modelling approach could be improved.

- Some parameters used for the bidomain equations such as the intra-cellular and extra-cellular conductivities are not based on experimental values. Their values are less than the conductivities in the cardiac tissue. This is in agreement with the findings of Blazeski *et. al* [6], where it has been shown that for hiPSC-CM the conduction velocity (CV) is much slower than in a normal human heart. However, this could be related to other factors that are not taken into account in our model, such as gap junctions. The values that we introduced have been chosen to fit the CV in the *in vitro* experiment.
- The heterogeneity of the hiPSC-CMs preparations has been modeled in a somehow arbitrary way, with mainly qualitative arguments. Even if an averaging procedure allows to limit the consequences of this arbitrariness, it would be more satisfactory to rely on a better experimental characterization of the phenotypes repartition in the monolayer model.
- The ionic model is not necessarily well adapted to the hiPSC-CMs used in the experiments, even if it was designed for stem cells. For instance, there is no description of late sodium current in the Paci model and this limitation moderates the results obtained on the effect of mexiletine on the field potential.
- When computing the different biomarkers quantities on the QRS and the repolarization wave, we only perform rate variability corrections when computing time intervals or delays. For the magnitude related biomarkers, the only correction that we introduce is to compute relative quantities with respect to the control case.

- The parameters used for the drug model, like the IC_{50} values, do not necessarily correspond to the parameters of hiPSC-CMs.

In spite of all these limitations, this multiscale approach, which combines physiologically detailed ionic models with the bidomain equations and a model of a MEA device, is able to reproduce the correct trends of the effect of drugs. It might therefore be a valuable tool to analyze the signals acquired by MEAs: given a series of measurements corresponding to different doses of a compound, parameter identification algorithms could be used to automatically identify which channels were affected. This is the object of an ongoing work.

5. Acknowledgments

This work was partially supported by the French National Agency of Research through the grant ANR-13-LAB1-0007 (LabCom “CardioXcomp”). We would like to thank Janssen Pharmaceutica NV for providing us with the raw data, and David Labarre, Fabien Raphel and Christophe Bleunven for many fruitful discussions and for their assistance to deal with the experimental data.

6. References

- [1] K. Takahashi, S. Yamanaka, Induction of pluripotent stem cells from mouse embryonic and adult fibroblast cultures by defined factors, *cell* 126 (4) (2006) 663–676.
- [2] A. Mangi, N. Noiseux, D. Kong, H. He, M. Rezvani, J. S. Ingwall, V. J. Dzau, Mesenchymal stem cells modified with akt prevent remodeling and restore performance of infarcted hearts, *Nature medicine* 9 (9) (2003) 1195–1201.
- [3] M. A. Laflamme, K. Y. Chen, A. V. Naumova, V. Muskheli, J. A. Fugate, S. K. Dupras, H. Reinecke, C. Xu, M. Hassanipour, S. Police, et al., Cardiomyocytes derived from human embryonic stem cells in pro-survival factors enhance function of infarcted rat hearts, *Nature biotechnology* 25 (9) (2007) 1015–1024.

- [4] M. X. Doss, J. M. Di Diego, R. Goodrow, Y. Wu, J. M. Cordeiro, V. Nesterenko, H. Barajas-Martínez, D. Hu, J. Urrutia, M. Desai, C. Antzelevitch, Maximum diastolic potential of human induced pluripotent stem cell-derived cardiomyocytes depends critically on *ikr*, *PloS one* 7 (7) (2012) e40288.
- [5] J. He, Y. Ma, Y. Lee, J. A. Thomson, T. J. Kamp, Human embryonic stem cells develop into multiple types of cardiac myocytes action potential characterization, *Circulation research* 93 (1) (2003) 32–39.
- [6] A. Blazeski, R. Zhu, D. Hunter, S. Weinberg, K. Boheler, E. Zambidis, L. Tung, Electrophysiological and contractile function of cardiomyocytes derived from human embryonic stem cells, *Progress in biophysics and molecular biology* 110 (2) (2012) 178–195.
- [7] S. Peng, A. E. Lacerda, G. E. Kirsch, A. M. Brown, A. Bruening-Wright, The action potential and comparative pharmacology of stem cell-derived human cardiomyocytes, *Journal of pharmacological and toxicological methods* 61 (3) (2010) 277–286.
- [8] C. Robertson, D. D. Tran, S. C. George, Concise review: Maturation phases of human pluripotent stem cell-derived cardiomyocytes, *Stem Cells* 31 (5) (2013) 829–837.
- [9] K. Harris, M. Aylott, Y. Cui, J. Louttit, N. McMahon, A. Sridhar, Comparison of electrophysiological data from human-induced pluripotent stem cell-derived cardiomyocytes to functional preclinical safety assays, *toxicological sciences* (2013) kft113.
- [10] S. R. Braam, L. Tertoolen, A. van de Stolpe, T. Meyer, R. Passier, C. L. Mummery, Prediction of drug-induced cardiotoxicity using human embryonic stem cell-derived cardiomyocytes, *Stem cell research* 4 (2) (2010) 107–116.
- [11] O. Caspi, I. Itzhaki, I. Kehat, A. Gepstein, G. Arbel, I. Huber, J. Satin, L. Gepstein, In vitro electrophysiological drug testing using human embryonic stem cell derived cardiomyocytes, *Stem cells and development* 18 (1) (2009) 161–172.

- [12] L. Bowler, K. Harris, D. Gavaghan, G. Mirams, Simulated micro-electrode array recordings from stem cell-derived cardiomyocytes, *Journal of Pharmacological and Toxicological Methods* 81 (2016) 380.
- [13] I. Cavero, J.-M. Guillon, V. Ballet, M. Clements, J.-F. Gerbeau, H. Holzgreffe, Comprehensive in vitro Proarrhythmia Assay (CiPA): Pending issues for successful validation and implementation, *Journal of Pharmacological and Toxicological Methods* doi:10.1016/j.vascn.2016.05.012. URL <https://hal.inria.fr/hal-01328481>
- [14] M. Boulakia, F. Raphel, P. Zitoun, J.-F. Gerbeau, Toward transmembrane potential estimation from in vitro multi-electrode field potentials using mathematical modeling, *Journal of Pharmacological and Toxicological Methods* 75 (2015) 168–169.
- [15] N. Zemzemi, M. Bernabeu, J. Saiz, J. Cooper, P. Pathmanathan, G. Mirams, J. Pitt-Francis, B. Rodriguez, Computational assessment of drug-induced effects on the electrocardiogram: from ion channel to body surface potentials, *British journal of pharmacology* 168 (3) (2013) 718–733.
- [16] T. Brennan, M. Fink, B. Rodriguez, Multiscale modelling of drug-induced effects on cardiac electrophysiological activity, *European Journal of Pharmaceutical Sciences* 36 (1) (2009) 62–77.
- [17] N. Zemzemi, B. Rodriguez, Effects of l-type calcium channel and human ether-a-go-go related gene blockers on the electrical activity of the human heart: a simulation study, *Europace* 17 (2) (2015) 326–333.
- [18] M. Paci, J. Hyttinen, K. Aalto-Setälä, S. Severi, Computational models of ventricular-and atrial-like human induced pluripotent stem cell derived cardiomyocytes, *Annals of biomedical engineering* 41 (11) (2013) 2334–2348.
- [19] multichannel systems, Microelectrode array (mea) manual, http://www.multichannelsystems.com/sites/multichannelsystems.com/files/documents/manuals/MEA_Manual.pdf.
- [20] P. Colli Franzone, L. F. Pavarino, S. Scacchi, *Mathematical cardiac electrophysiology*, Vol. 13, Springer, 2014.

- [21] J. Sundnes, G. T. Lines, X. Cai, B. F. Nielsen, K. Mardal, A. Tveito, Computing the electrical activity in the heart, Vol. 1, Springer, 2007.
- [22] B. Hille, Ion channels of excitable membranes, Vol. 507, Sinauer Sunderland, MA, 2001.
- [23] C. Moulin, A. Glière, D. Barbier, S. Joucla, B. Yvert, P. Mailley, R. Guillemaud, A new 3-d finite-element model based on thin-film approximation for microelectrode array recording of extracellular action potential, Biomedical Engineering, IEEE Transactions on 55 (2) (2008) 683–692.
- [24] J. Sundnes, G. T. Lines, A. Tveito, An operator splitting method for solving the bidomain equations coupled to a volume conductor model for the torso, Mathematical biosciences 194 (2) (2005) 233–248.
- [25] R. Gulrajani, M.-C. Trudel, L. Leon, A membrane-based computer heart model employing parallel processing, Biomedizinische Technik/Biomedical Engineering 46 (s2) (2001) 20–22.
- [26] M. Pekkanen-Mattila, H. Chapman, E. Kerkelä, R. Suuronen, H. Skottman, A. Koivisto, K. Aalto-Setälä, Human embryonic stem cell-derived cardiomyocytes: demonstration of a portion of cardiac cells with fairly mature electrical phenotype, Experimental Biology and Medicine 235 (4) (2010) 522–530.
- [27] E. Carmeliet, K. Mubagwa, Antiarrhythmic drugs and cardiac ion channels: mechanisms of action, Progress in biophysics and molecular biology 70 (1) (1998) 1–72.
- [28] G. Mirams, M. Davies, Y. Cui, P. Kohl, D. Noble, Application of cardiac electrophysiology simulations to pro-arrhythmic safety testing, British journal of pharmacology 167 (5) (2012) 932–945.
- [29] G. Mirams, Y. Cui, A. Sher, M. Fink, J. Cooper, B. Heath, N. McMahon, D. Gavaghan, D. Noble, Simulation of multiple ion channel block provides improved early prediction of compounds clinical torsadogenic risk, Cardiovascular research 91 (1) (2011) 53–61.

- [30] D. Bottino, R. C. Penland, A. Stamps, M. Traebert, B. Dumotier, A. Georgieva, G. Helmlinger, G. S. Lett, Preclinical cardiac safety assessment of pharmaceutical compounds using an integrated systems-based computer model of the heart, *Progress in biophysics and molecular biology* 90 (1) (2006) 414–443.
- [31] M. Paci, S. Severi, J. Hyttinen, Computational modeling supports induced pluripotent stem cell-derived cardiomyocytes reliability as a model for human *Iqt3*, in: *Computing in Cardiology Conference (CinC)*, 2014, IEEE, 2014, pp. 69–72.
- [32] Y. Qu, H. M. Vargas, Proarrhythmia risk assessment in human induced pluripotent stem cell-derived cardiomyocytes using the maestro mea platform, *Toxicological Sciences* 147 (1) (2015) 286–295.
- [33] A. Zahradníková, I. Minarovič, I. Zahradník, Competitive and cooperative effects of bay k8644 on the l-type calcium channel current inhibition by calcium channel antagonists, *Journal of Pharmacology and Experimental Therapeutics* 322 (2) (2007) 638–645.
- [34] A. Bucchi, M. Baruscotti, M. Nardini, A. Barbuti, S. Micheloni, M. Bolognesi, D. DiFrancesco, Identification of the molecular site of ivabradine binding to *hcn4* channels, *PloS one* 8 (1) (2013) e53132.